

STATIC AND DYNAMIC PRESSURE DISTRIBUTIONS IN A SHORT LABYRINTH SEAL

K.T. Millsaps and M. Martinez-Sanchez
Massachusetts Institute of Technology
Gas Turbine Laboratory
Cambridge, Massachusetts 02139, U.S.A.

1. Introduction

Although important progress has been made in the last few years on the understanding of labyrinth seal fluid mechanics, and in particular, on the generation of side forces by such seals, there is still a need for quantitative data and theoretical correlation on several points, particularly with respect to dynamic effects. The widely quoted test results of Benckert and Wachter [1] covered adequately a range of flow and geometric parameters, but only for static offsets. Good correlation to linearized theory has been achieved for these data [2], [3]. Several authors have reported measurements of a dynamic nature [4], [5], [6], [7], but their tests lacked control over important parameters, making comparison to theory difficult. Scharrer and Childs [8] presented the first set of dynamic data in which inlet swirl as well as vibratory frequency were adequately controlled, although a single shaking frequency was used. They reported directly measured force data for three 16-tooth rotors with different sealing clearances, and obtained good correlation to theory on the effect of some of the parameters.

No data of this type have been obtained for short (one or two cavity) seals, of interest in aerospace applications, including turbine tip shrouds. There are also no published data (static or dynamic) on labyrinth seals with honeycomb land.

As part of an investigation into turbine blade-tip destabilizing forces, sponsored by NASA Marshall SFC, we have built a seals test rig in which spin rate, circular whirl rate, direction and amplitude of inlet swirl angle, and eccentricity can all be controlled over wide ranges, and measurements can be made at gap Reynolds numbers up to about 2×10^4 (previous data have been limited to well below 10^4). In this paper, we describe this facility and present preliminary data for a one-cavity labyrinth seal with a flat, stator-mounted land.

2. Test Facility

Tests are conducted using air in an open loop with atmospheric discharge. The overall layout is shown in Fig. 1. The test rotor is forced to execute a circular whirl motion while spinning. This is accomplished by mounting the rotor shaft bearings eccentrically on an inner rotating assembly (Fig. 2), which is driven by a belt independently of the in-line rotation drive. The rotating parts are shown in Fig. 3. The test seal is mounted on the left-hand rotor (28 cm diameter), with seal air flow being from left to right. Pressurized air is also introduced behind this rotor to balance the thrust. The pulley sheaf for the whirl drive can be seen at the right-hand end of the rotating housing. Variable amounts of shaft eccentricity can be introduced by appropriate rotation of eccentric inserts placed between the rotating bearing housing and the outer bearing races (Fig. 4).

Pressurized air is fed from an annular plenum through replaceable swirl vane rings into the pre-seal cavity (Fig. 3). Close spacing of the vanes is used to ensure azimuthal uniformity. The convergence in the vane passage imparts high velocity, and hence high azimuthal momentum, to the inlet flow. Flow swirl angles from zero to about 60° can be generated in this way.

The main data obtained are pressure time histories at four points (90° spaced) in the gland. These are acquired by flush-mounted, fast response Kulite XCS-190 transducers, which have a 5 psid range. To increase the response sensitivity, the transducers are referenced to an auxiliary pressure-averaging plenum, which is connected by thin tubes to several points on the gland and is filled with a porous material for damping purposes. In this way, only the necessary pressure non-uniformity component is measured.

Rotor displacements are measured to within ± 0.1 mil by two orthogonally mounted Bently Nevada CSN-5 proximeters. Other measurements include flow rate, using a Venturi flow meter, and accelerometer data, mainly for health monitoring purposes. The spin and whirl motors are velocity controllable, in both directions, ± 6000 RPM for spin and ± 3000 RPM for whirl.

The transducer data are digitized at up to 10 kHz by a 12-bit, 32-channel Lecroy A/D converter, and then stored in a computer disc. 256 whirl orbits are acquired and phase-lock averaged in each test, using synchronizing signals derived from two photocell-photodiode pairs in combination with a chopper wheel. This gives 32 averaged samples per whirl orbit from each transducer. Fitting a cosine curve to these data allows calculation of both components of the pressure force acting on the rotor, and rotating in space at the whirl frequency. In principle, any one of the four transducers would suffice for this; the others provide redundancy and cross-checking. A typical trace of raw voltage vs. angular location in the whirl cycle for one of the pressure channels is shown in Fig. 5. Most of the noise is effectively removed by the averaging procedure as shown in Fig. 6.

The approximate range of parameters that can be covered with this facility is shown in Fig. 7 for a seal with 10 mm cavity length, as used in this study. The left-hand boundary is a line of Reynolds number (based on gap and gap flow velocity) equal to 10^4 . This is not, however, a hard limit and, as noted, many experimenters have worked below it. For rocket turbopump applications, however, we do wish to operate above this range to avoid complications with the transition regime of the discharge coefficient. The right-hand boundary is a value of order unity for the parameter K , defined as $K = \ell \tan^6 \theta / \delta$ (ℓ = gland length, δ = mean gap). For too small values of K , the exit gap is larger than the jet width from the first gap, and excessive carry-over is expected. Clearly, use of a longer seal will allow correspondingly wider gap sizes, hence higher Reynolds numbers for a given pressure ratio; lengths up to about 1.8 cm can be easily accommodated.

The upper boundary in Fig. 7 corresponds to choked exit flow. Again, this is not a hard limit, but we wish to restrict attention to the subsonic regime of interest for shroud seals in low pressure ratio turbopump turbines.

3. Experimental Results

The range of parameters used in the tests reported here is listed in Table 1. Figures 8 and 9 show the direct and cross-forces calculated from the measured pressure distributions, using the gland length times the seal perimeter as the effective area for integration. The data in Figs. 8 and 9 are for zero rotor spin. The forces are presented vs. whirl speed (positive in the pre-swirl direction) and pre-swirl vane angle. For the direct forces (Fig. 8), positive sign indicates a force in the direction opposite that of the rotor displacement. For the cross-forces (Fig. 9), positive sign indicates a force tending to drive forward whirl, i.e. in the pre-swirl direction. Data are presented for inlet swirl angles of 0°, 15°, and 30°. For zero inlet swirl, the direct force is almost independent of whirl frequency as is predicted by theory. The direct force decreases with inlet swirl.

The cross-force increases with inlet swirl and decreases with whirl speed. Figure 10 shows cross-force vs. whirl RPM with no inlet swirl or shaft rotation for three different inlet pressures (mass

flow rates). The forces increase with flow rate. Figure 11 shows the same cross-force but now normalized by the ratio of flow rate to design flow. Notice that the data are collapsed to a single curve. This also works quite well for the direct forces. The reason for this is that the magnitude of the pressure wave scales with mass flow but the relative phase (the angle between the minimum whirling gap and the maximum pressure) is virtually independent of flow for a given whirl speed. This is the case for zero inlet swirl. However, when inlet swirl exists, the theory suggests that the flow normalized forces should be plotted vs. a reduced whirl speed if they are to effectively collapse. One possible whirl parameter is $\Omega \cdot R_s / V_i$, where Ω is the whirl speed (rads/sec), R_s is the seal radius, and V_i is the inlet swirl velocity.

Once cross-force vs. whirl is available, the cross-stiffness and direct damping coefficients are readily obtained. A least squares linear curve fit is used to obtain the zero-frequency crossing. This is the cross-stiffness K_{xy} . Figure 12 shows K_{xy} vs. inlet swirl angle for several different seal rotation speeds. In general, it is seen that rotation in the direction of pre-swirl tends to reduce the cross-stiffness, while rotation in the direction opposite that of swirl tends to increase the zero-frequency force. The direct damping, C_{xx} , is the slope of the cross-force vs. whirl curve fit line. Figure 13 shows the direct damping vs. inlet swirl angle for several different seal rotation speeds. The damping generally increases with swirl inlet velocity. The spin rate is seen to have a substantial impact on both stiffness and damping coefficient.

4. Discussion

The data were compared to theoretical predictions based on a lumped parameter Kostyuk-Iwatsubo type model [2], [9]. Briefly, the continuity and momentum equations for the single gland labyrinth are first solved for the centered position. These steady state parameters are used in a linear perturbation expansion. When harmonic behavior is assumed, a system of linear algebraic equations in pressure and velocity perturbations are obtained (see Ref. [9] for details). These are solved to yield the pressure amplitude and phase relative to the minimum whirling gap. The actual computations were done in non-dimensional form. The dimensionless parameters which introduce the most uncertainty are the flow coefficients μ_1 and μ_2 for the first and second knife, respectively. In general, μ_2 is greater than μ_1 due to the kinetic energy carry-over. Let the effective flow area divergence be defined by

$$\alpha = \frac{\mu_2 \delta_2^*}{\mu_1 \delta_1^*} \quad (1)$$

For $\alpha = 1$, theory indicates zero direct force (for zero preswirl, spin, and whirl). It is clear, however, from Fig. 8, that a significant direct force does exist for this case. One possible explanation for this is the large sensitivity of direct forces to small departures of α from unity. In fact, the value of α required to explain the data can be extracted from the theoretical [9] direct force for zero spin, whirl, and swirl:

$$F_d = \pi R_s \ell \frac{\alpha(\alpha-1)}{(1+\alpha^2)^{3/2}} \frac{P_i^2 - P_e^2}{\sqrt{P_i^2 + \alpha^2 P_e^2}} \frac{r}{\delta^*} \quad (2)$$

where R_s is the seal radius, ℓ the gland length, P_i and P_e are the inlet and discharge pressures, r is the eccentricity and δ^* the nominal gap. We obtain from Eq. (2) and Fig. 8 the value $\alpha = 1.113$.

On the other hand, α has only a very minor effect on the cross-forces according to theory. An equivalent statement is that, as α varies, there are significant effects on the spatial phase angle of the forces, and somewhat less on the force magnitude, while the cross-force component changes little. Thus, our direct data on phase angle can be also used to extract α , and the range is indeed found to be 1.1 to 1.2.

Referring to Figs. 9 and 13, the data for zero inlet swirl and zero spin indicate non-zero damping, C_{xx} (slope of cross-force vs. whirl), although with zero cross-force at zero whirl ($K_{xy} = 0$). The linear theory predicts these features. In particular, the predicted C_{xx} at zero whirl is 17 N sec/m, while the data (Fig. 13) indicate 23 N sec/m.

Figure 14 shows a comparison of the cross-force data to linearized theory for zero spin, 30° inlet swirl. The zero-frequency crossing (K_{xy}) is well predicted, while the data show once again a larger slope (more damping) than theory indicates. The agreement as to K_{xy} is worse for 15° since, as shown in Fig. 9, there is an as yet unexplained non-linearity of cross-force versus swirl. This may be a result of the inlet swirl being significantly different from its design value, a circumstance that needs to be verified.

5. Conclusions

The Labyrinth Seal Test Facility, which has been built to cover a wide range of test conditions not previously obtained, has been completed and is fully operational. Rotordynamic coefficient measurements for a single gland labyrinth seal were made for many different flow rates, whirl speeds, shaft speeds, and inlet swirls. To the authors' knowledge, these are the first such controlled measurements for either a single gland or at a Reynolds number above transition (10^4). There is reasonable agreement between the experimentally obtained data and the simple Kostyuk-Iwatsubo Theory. However, many more comparisons over a wider range of parameters is necessary. The impact of different flow coefficients for the first and second knives on the rotordynamic coefficients has been found. While this effect is dominant for the direct forces, it should also be incorporated into calculations of cross-forces where it has an impact under many conditions.

References

1. Benckert, H. and Wachter, J., "Flow-Induced Coefficients of Labyrinth Seals," NASA CP-2133, May 1980.
2. Lee, O.K., Martinez-Sanchez, M. and Czajkowski, E., "Prediction of Force Coefficients for Labyrinth Seals," NASA CP-2338, 1984, pp. 235-256.
3. Scharrer, J.K. and Childs, D.W., "An Iwatsubo-Based Solution for Labyrinth Seals: A Comparison to Experimental Results," *J. of Gas Turbines and Power*, Vol. 108, April 1986, pp. 325-331.
4. Wright, D.V., "Labyrinth Seal Forces on a Whirling Rotor," *Rotor Dynamic Instability*, Proceedings of the ASME Applied Mech., Bioeng. and Fluids Engineering Conf., Houston, TX, 1983, pp. 19-31.
5. Iwatsubo, T., Matsuoka, N. and Kawai, R., "Flow-Induced Force and Flow Pattern of Labyrinth Seals," NASA CP-2133, 1982, pp. 205-222.
6. Brown, R.D. and Leong, Y.M.M.S., "Experimental Investigation of Lateral Forces Induced by Flow Through Model Labyrinth Glands," NASA CP-2338, 1984, pp. 187-210.

7. Hisa, S., "Steam Excited Vibrations in Rotor-Bearing Systems," *Proc. of the International Conf. on Rotordynamics*, Tokyo, Japan, Sept. 1986, pp. 635-641.
8. Childs, D.W. and Scharrer, J.K., "Theory vs. Experiment for the Rotordynamic Coefficients of Labyrinth Gas Seals: Part II-A, Comparison to Experiment," *ASME Rotating Machinery Dynamics*, Vol. 1, 1987, pp. 427-434.
9. Millsaps, K.T., "Analysis of Aero-Elastic Forces in Labyrinth Seals and the Design of an Experimental Facility to Measure Them," Master's Thesis, Department of Aeronautics and Astronautics, MIT, 1987.

TABLE 1
OPERATING PARAMETERS FOR THIS WORK

Seal Radius	150 mm
Number of Seal Glands	1
Gland Length	10 mm
Dam Height	5 mm
Type of Land	Flat, on stator
Mean Seal Gap	0.813 mm
Seal Eccentricity	0.185 mm
Inlet Total Pressure	1.48 to 1.69 atm
Discharge Pressure	1 atm
Air Temperature	280°K
Inlet Swirl Angle	0°, 15°, 30°
Whirl Speed	-2500 to +2500 RPM
Spinning Rate	-4200 to +4200 RPM

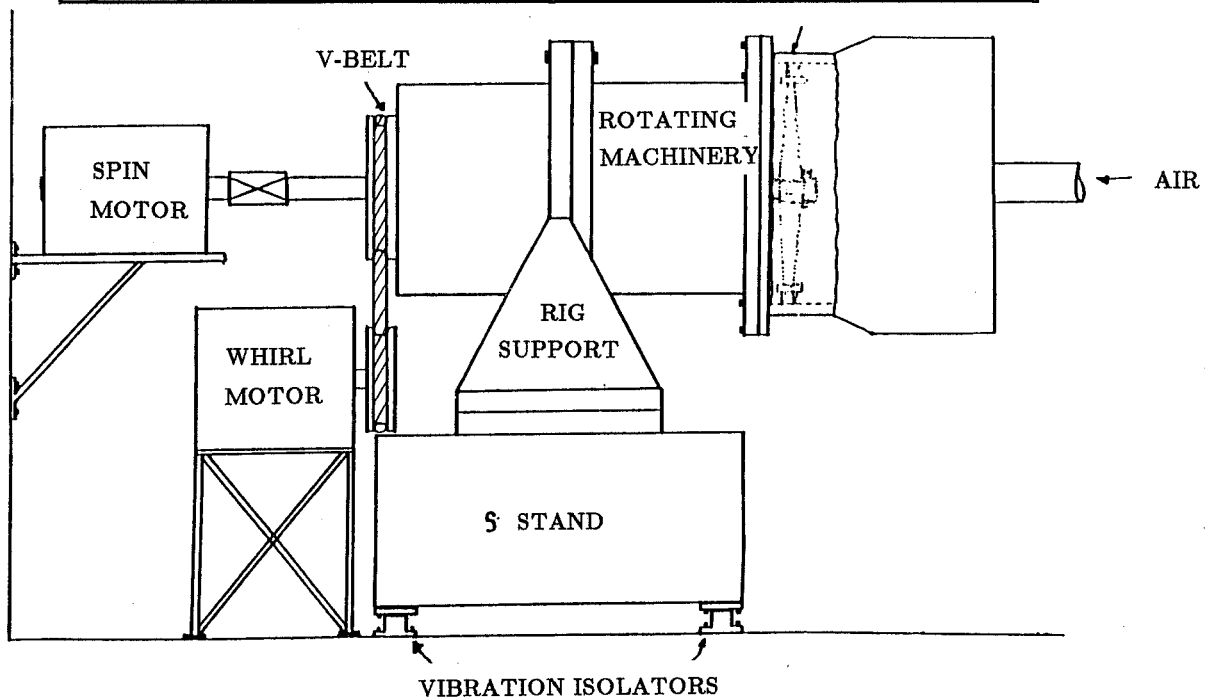


Figure 1. Side view of labyrinth seal test facility.

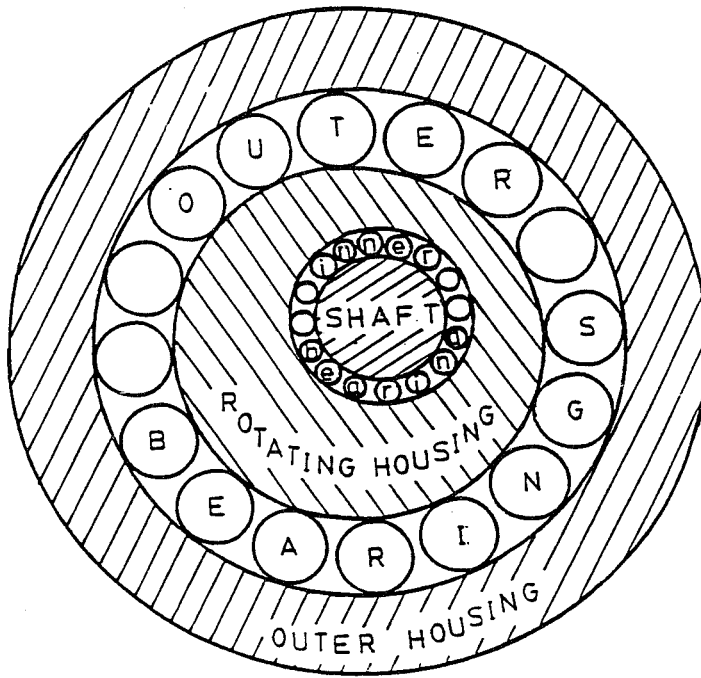


Figure 2. Mechanism for producing spinning/whirling shaft.

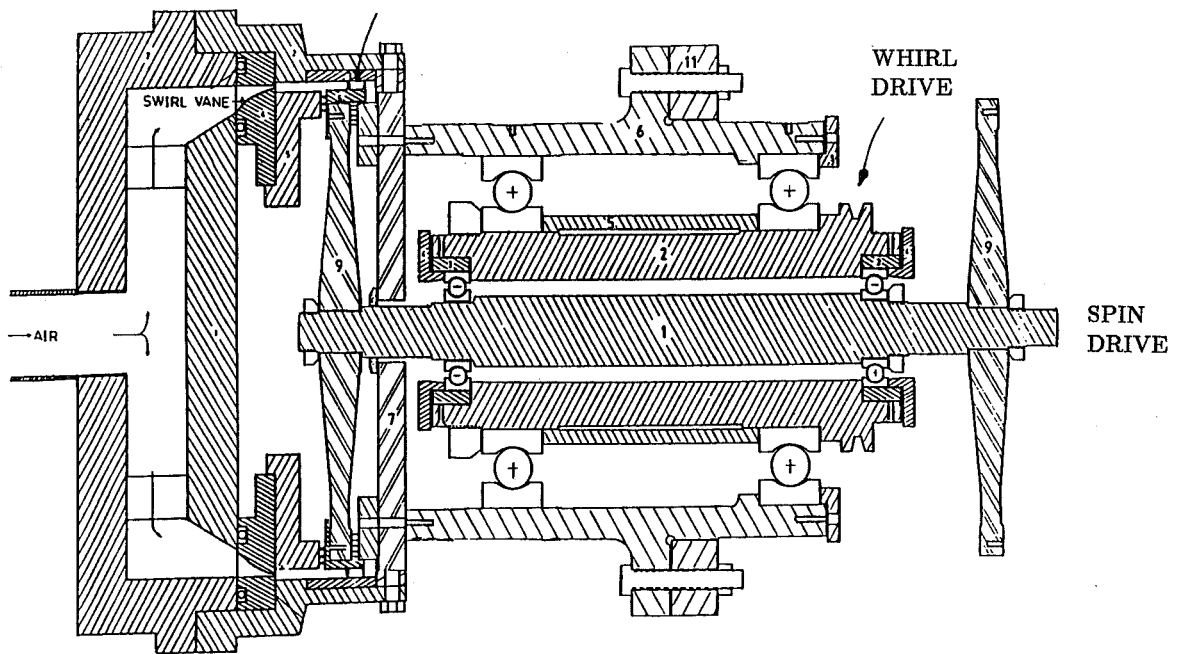


Figure 3. Cross-section of test section along with whirl/spin producing rotating machinery. The air flow through the apparatus is shown by arrows.

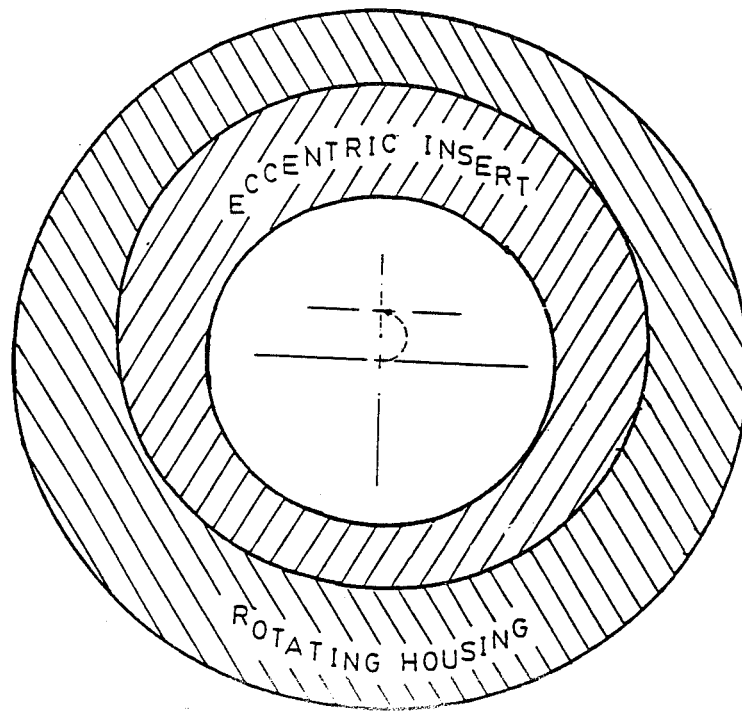


Figure 4. Mechanism for producing variable whirl eccentricity.

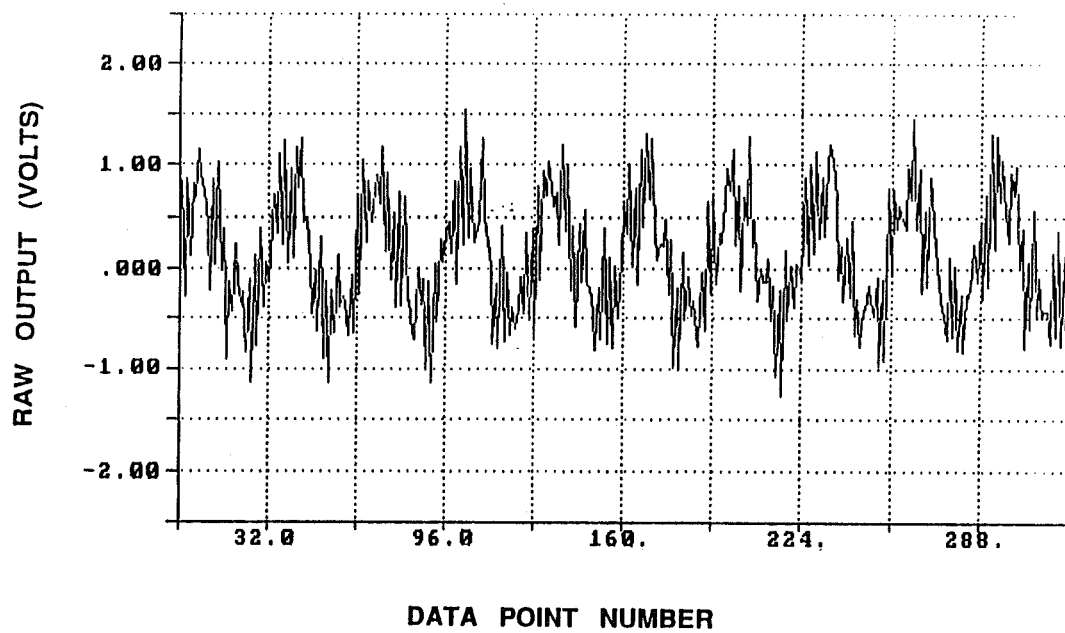


Figure 5. Raw voltage from a Kulite vs. data point number.

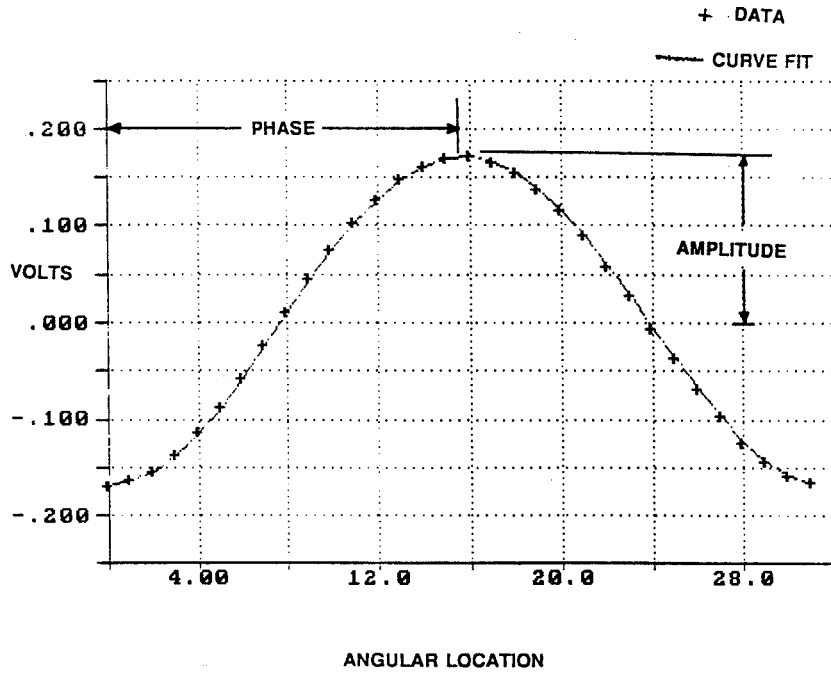


Figure 6. Typical 4 transducer composite phase-locked average pressure data along with least squares curve fit.

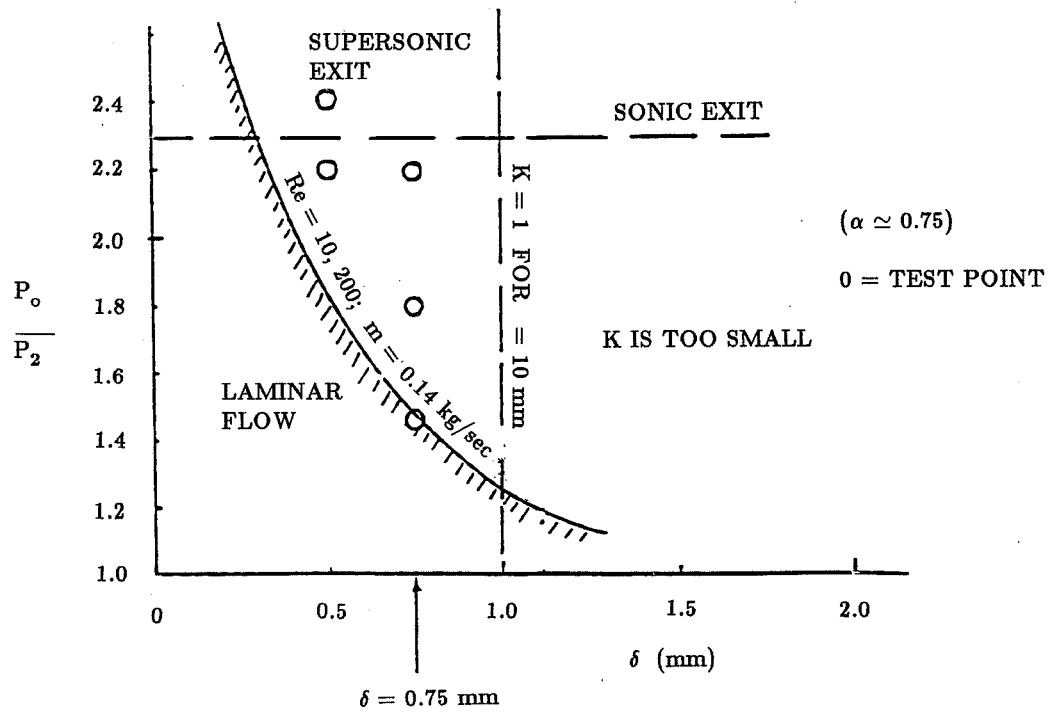


Figure 7. Approximate operational boundaries for test seal with $l=10\text{mm}$.

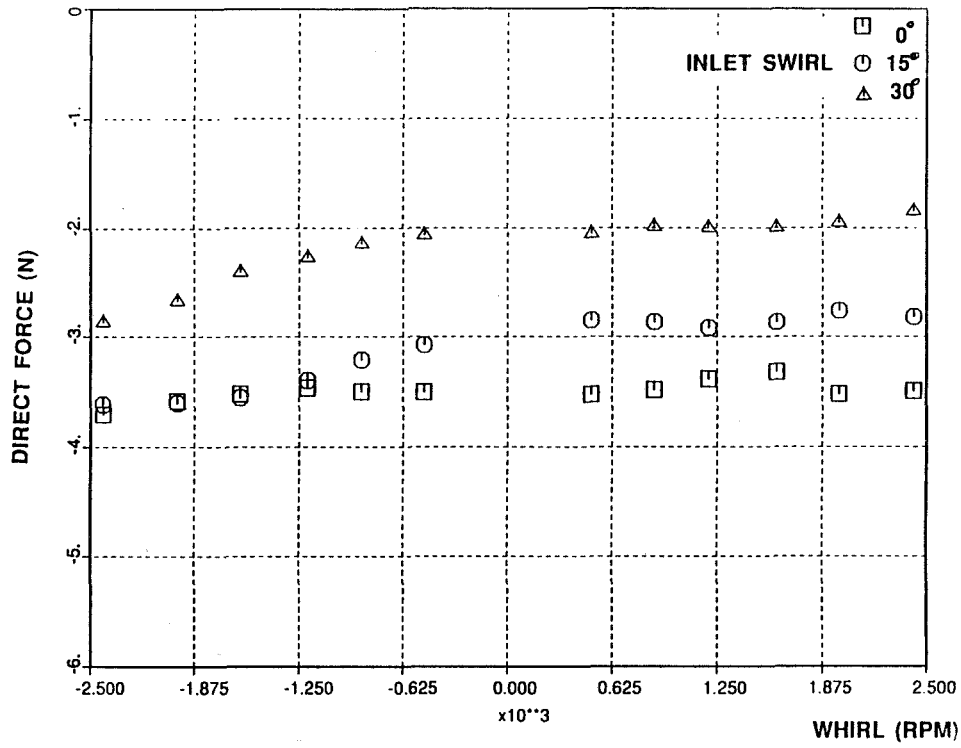


Figure 8. Direct force vs. whirl RPM for three different values of inlet swirl.
 $m=0.166$ kg/s.

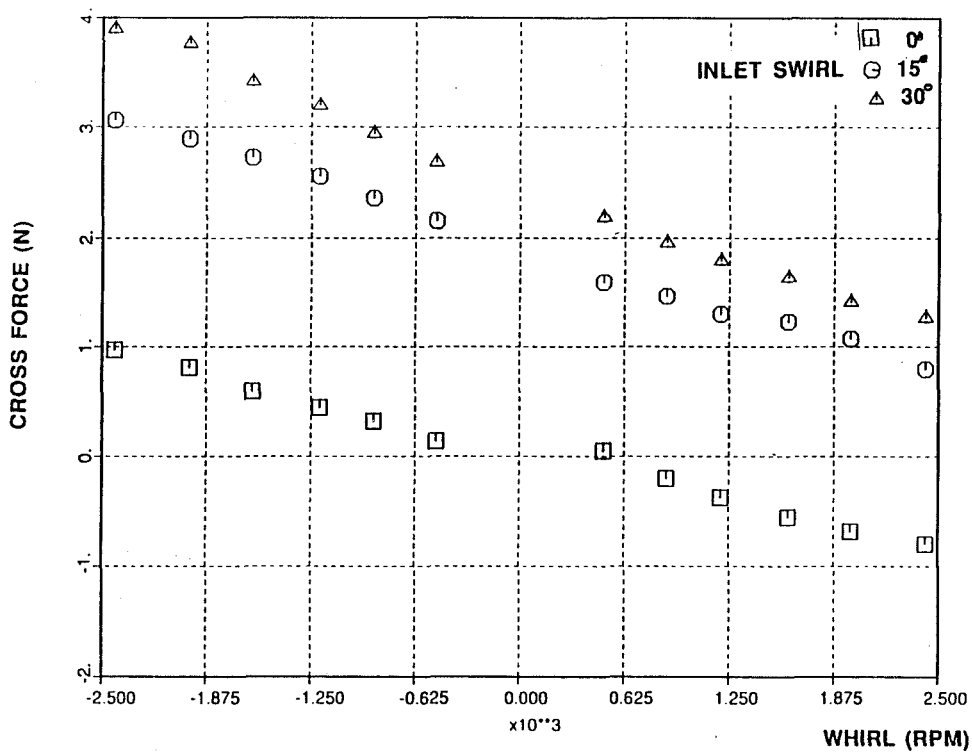


Figure 9. Cross-force vs. whirl RPM for three different values of inlet swirl.
 $m=0.166$ kg/s.

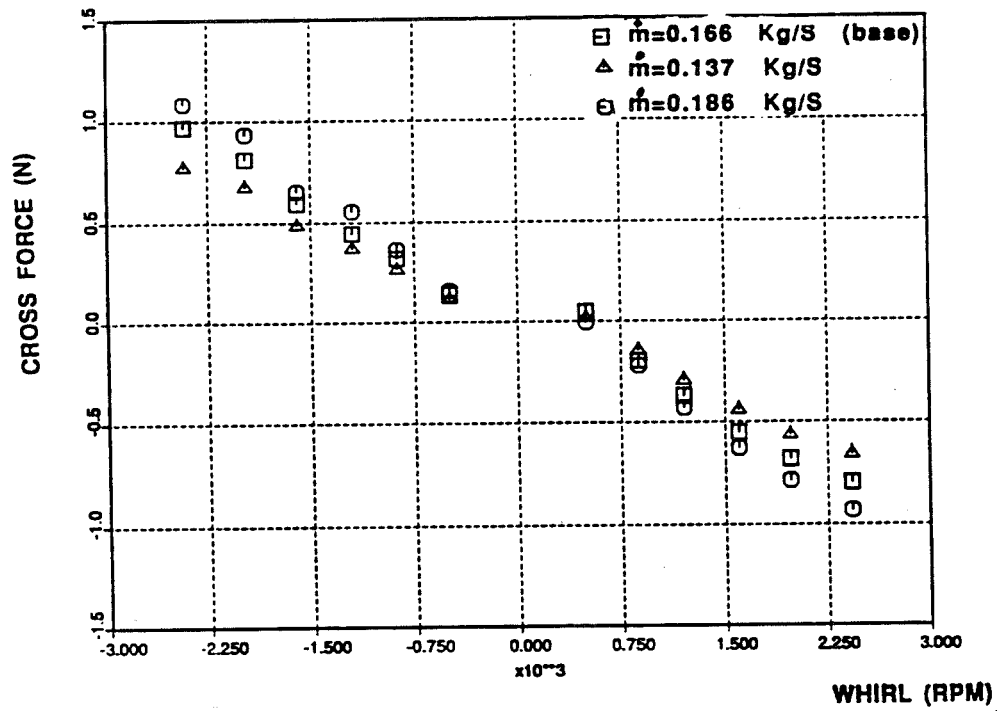


Figure 10. Cross force vs. whirl RPM for three different mass flow rates. All conditions are with no inlet swirl or shaft rotation.

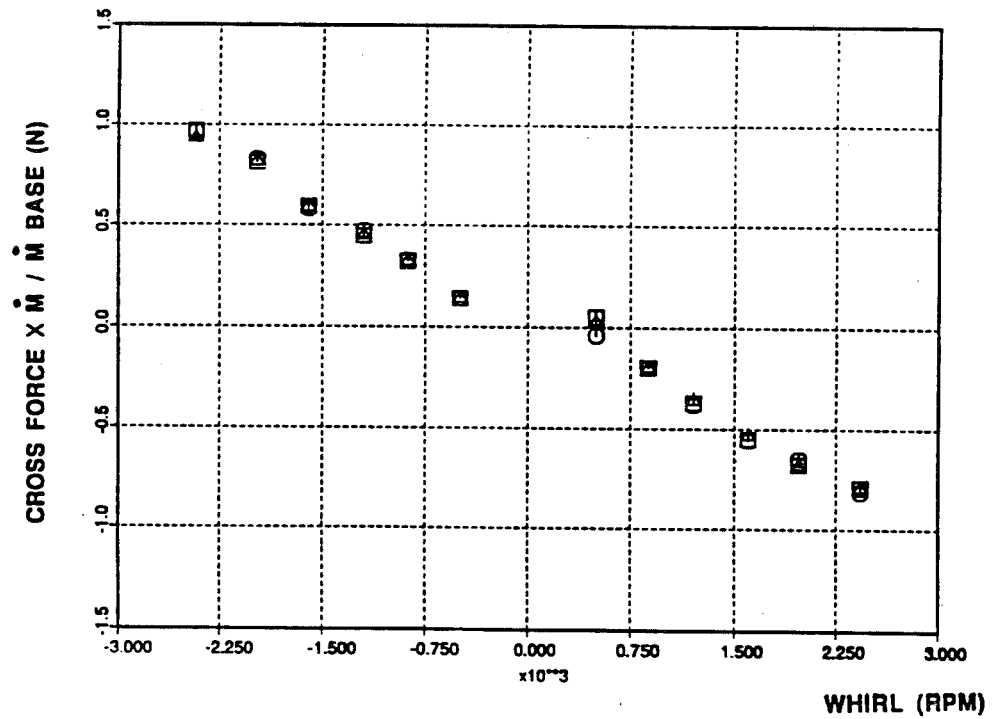


Figure 11. Cross force, normalized by the base mass flow vs whirl RPM. This is the same data as shown above.

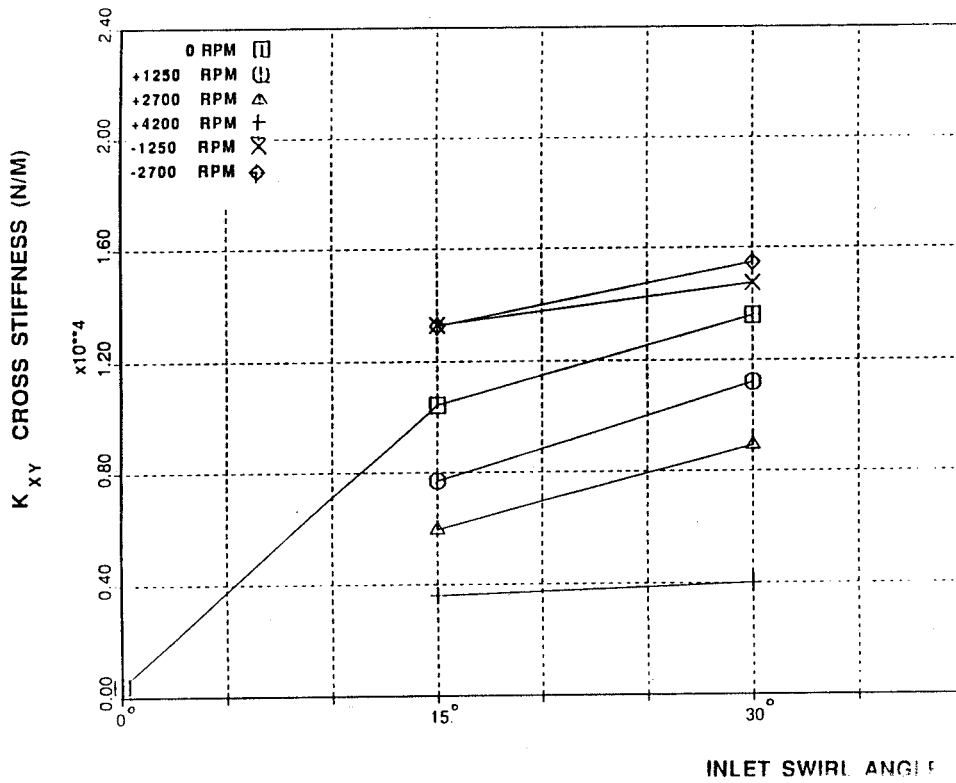


Figure 12. Cross stiffness vs. inlet swirl for six different values of spin.
 $m=0.166$ kg/s.

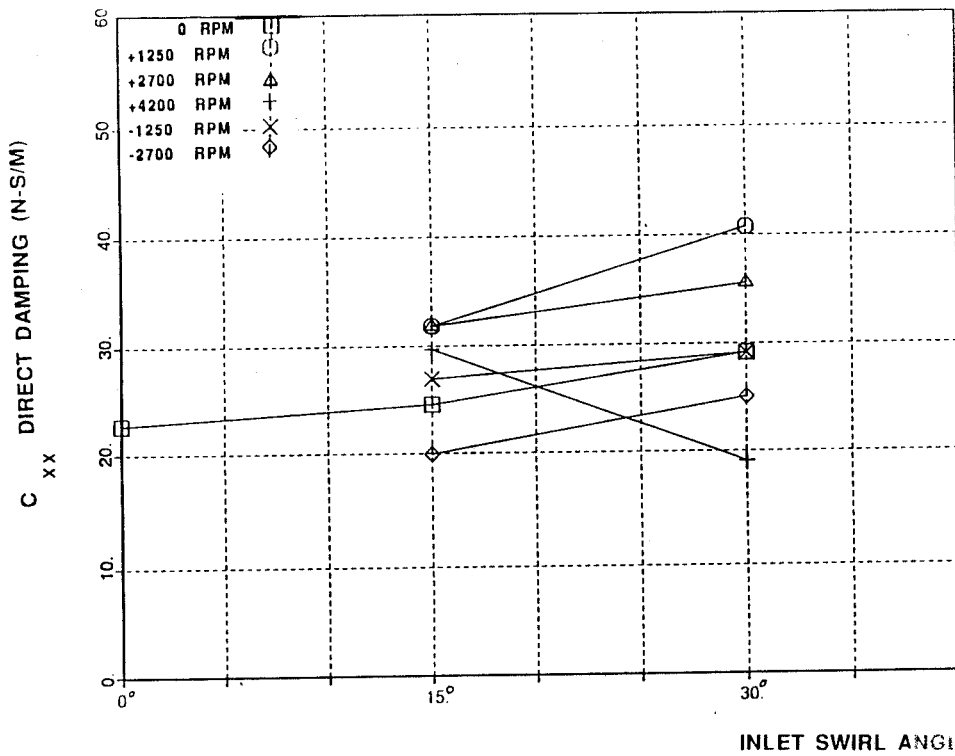


Figure 13. Direct damping vs. inlet swirl for six different values of spin.
 $m=0.166$ kg/s.

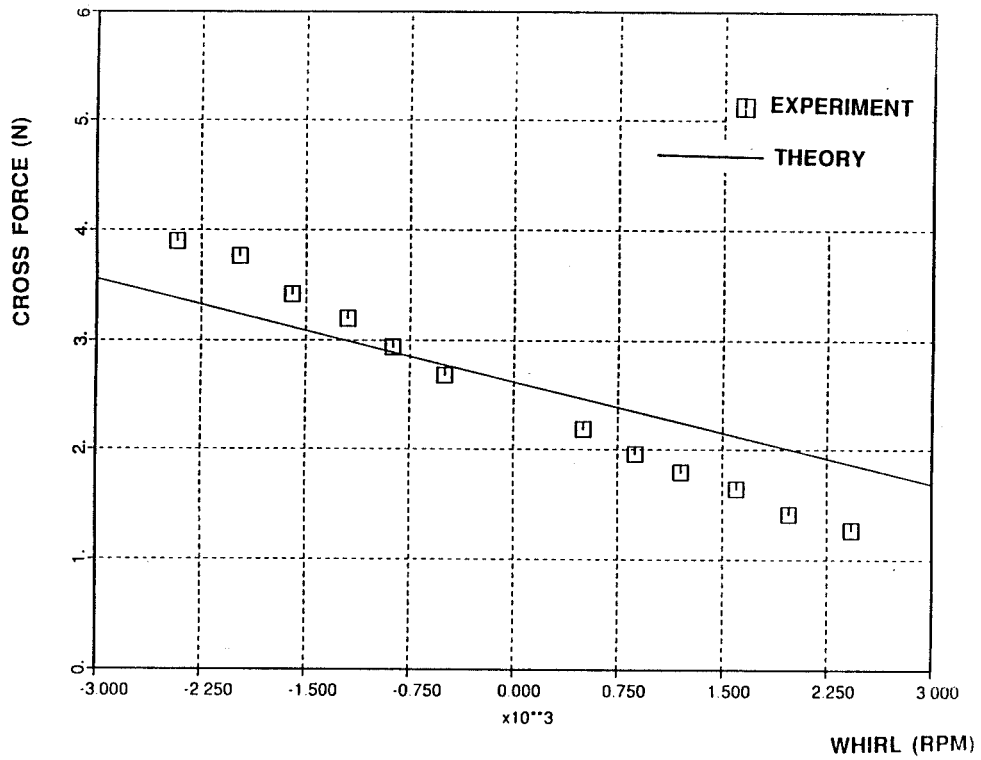


Figure 14. Comparison of experimental data with theory. The inlet swirl for this case is 30 degrees and the mass flow is 0.166 kg/s.